Journal of Materials Chemistry C

ROYAL SOCIETY OF CHEMISTRY

PAPER

View Article Online
View Journal | View Issue

Cite this: J. Mater. Chem. C, 2022, 10, 4805

Aromatic-imide-based TADF enantiomers for efficient circularly polarized electroluminescence†

Yin-Feng Wang,‡[ab] Xun Liu,‡[c] Yongheng Zhu,[c] Meng Li *[a] and Chuan-Feng Chen *[ab]

Received 13th October 2021,
Accepted 1st January 2022

DOI: 10.1039/d1tc04893g

rsc.li/materials-c

Recently, much attention has been paid to circularly polarized organic light-emitting diodes (CP-OLEDs) based on thermally activated delayed fluorescence (TADF) enantiomers. In this paper, we designed and synthesized a pair of aromatic-imide-based TADF enantiomers, namely *R*/*S*-**OBN-AICz**, using chiral perturbation strategy. The chiral emitters concurrently demonstrated efficient TADF and aggregation-induced emission (AIE) properties, together with a small singlet–triplet energy gap (ΔE_{ST}) of 0.08 eV and a high photoluminescence quantum yield (PLQY) of 81%. Moreover, the TADF enantiomers exhibited clear circularly polarized luminescence (CPL) activities with dissymmetry factor ($|g_{PL}|$) values of up to 2.6×10^{-3} in toluene solution. Finally, the TADF enantiomers were utilized as emitters to fabricate CP-OLEDs, which achieved clear circularly polarized electroluminescence (CPEL) signals, a high maximum external quantum efficiency (EQE_{max}) of 19.0% and a high maximum luminance (L_{max}) of 24 790 cd m^{-2}.

Introduction

Recently, circularly polarized luminescence (CPL) materials have attracted more and more attention for their extensive application prospects in the fields of anti-glare displays, 3D displays, encrypted transmission, optical communications, optical recognition sensing, quantum computing, and so on.[1] So far, CP photoluminescence (CPPL) has been extensively studied, but CP electroluminescence (CPEL), a more valuable property for optoelectronic technology in the future, is still in its infancy.[2] The organic light-emitting diode (OLED), as one of the most successful electroluminescent devices, has many advantages such as high resolution, high flexibility, high electroluminescence efficiency and low power consumption.[3] Therefore, circularly polarized OLEDs (CP-OLEDs) fabricated with a chiral emitter are considered to be a promising strategy for realizing CPEL.[4] Since the first case of CP-OLEDs was reported in 1997,[5] a variety of chiral emitters suitable for CP-OLEDs have been developed, including chiral fluorescent emitters,[6] chiral phosphorescent emitters,[7] and chiral thermally activated delayed fluorescent (TADF) emitters.[8] Compared with the first two kinds of chiral emitter, chiral TADF emitters have been more widely used to fabricate efficient CP-OLEDs in recent years[9] owing to their purely organic molecular structures and theoretical 100% internal quantum efficiencies.[10] Thus, the development of new chiral TADF molecules is the key issue for obtaining highly efficient CPEL.

The chiral perturbation strategy, which directly combines chiral units and TADF skeletons, is the main method used to design chiral TADF emitters. Thus, it is important to develop such proper chiral moieties and efficient TADF moieties. For chiral moieties, three common moieties, including cyclohexanediamine,[11] binaphthol[12] and octahydro-binaphthol (OBN), have been used.[13] Among these, OBN is an excellent chiral unit due to its good solubility and chiral stability. Zheng's group[13a,b] developed two pairs of TADF enantiomers by merging chiral OBN moieties with effective cyan acceptor-based TADF skeletons and achieved CPEL and high efficiencies in both doped and non-doped CP-OLEDs. Later, Li *et al.*[13c] introduced OBN units into the multiple resonance TADF units to achieve CPEL as well as narrowband emission. More recently, Tang and co-workers[13d] fabricated a series of red CP-OLEDs using chiral OBN-based TADF emitters. Therefore, it is feasible and convenient to construct chiral TADF molecules *via* the chiral perturbation strategy using OBN as a chiral moiety.

In recent years, we have devoted attention to expanding the chiral aromatic-imide family and have reported some successful attempts.[14] In this work, (*R*/*S*)-OBN chiral units were

[a] Beijing National Laboratory for Molecular Sciences, CAS Key Laboratory of Molecular Recognition and Function, Institute of Chemistry, Chinese Academy of Sciences, Beijing, 100190, China. E-mail: cchen@iccas.ac.cn, limeng@iccas.ac.cn
[b] University of Chinese Academy of Sciences, Beijing, 100049, China
[c] College of Food Science and Technology, Shanghai Ocean University, Shanghai, 201306, China

† Electronic supplementary information (ESI) available. CCDC 2107122. For ESI and crystallographic data in CIF or other electronic format see DOI: 10.1039/d1tc04893g

‡ The authors contributed equally to the creation of this work.

introduced into aromatic-imide-based TADF skeletons to develop TADF enantiomers *R*/*S*-**OBN-AICz**. The obtained chiral aromatic-imide displayed a highly twisted conformation and a large torsion angle between the donor and acceptor, leading to a small singlet–triplet energy gap (ΔE_{ST}) of 0.08 eV and efficient TADF properties. Meanwhile, the TADF enantiomers showed intense CPL signals with dissymmetry factor ($|g_{PL}|$) values of 2.6×10^{-3}, a high photoluminescence quantum yield (PLQY) of 81%, as well as aggregation-induced emission (AIE) properties. Moreover, using the *R*/*S*-**OBN-AICz** enantiomers as emitters, the resulting CP-OLEDs exhibited an excellent device performance with maximum external quantum efficiency (EQE_{max}), current efficiency (CE_{max}), power efficiency (PE_{max}), and maximum luminance (L_{max}) values of 19.0%, 55.9 cd A^{-1}, 47.5 lm W^{-1}, and 24790 cd m^{-2}, respectively. Besides, the devices showed noticeable CPEL signals.

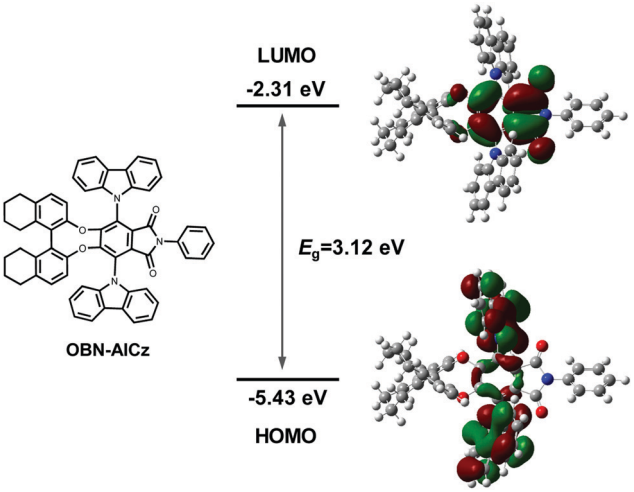

Fig. 1 Chemical structures and calculated HOMO/LUMO distributions of **OBN-AICz**.

Results and discussion

Synthesis, theoretical calculations, single-crystal analysis and electrochemical properties

The synthetic routes to a pair of enantiomerically pure TADF emitters *R*/*S*-**OBN-AICz** are shown in Scheme 1. **AI-4F** was prepared according to the method reported by our group.[15] Then, the *R*/*S*-**OBN-AI2F** intermediates were synthesized simultaneously through the nucleophilic substitution reaction of (*R*/*S*)-octahydro-binaphthol and **AI-4F**. The final products were obtained *via* nucleophilic substitution from carbazoles and the *R*/*S*-**OBN-AI2F** chiral intermediates. All the new molecules were characterized *via* their ^{1}H NMR, ^{13}C NMR and high-resolution mass spectra.

To gain insight into the electronic distributions and energy levels of **OBN-AICz**, density functional theory (DFT) calculations were performed using the Gaussian 09 package at the B3LYP/6-31G(d) level. As shown in Fig. 1, the lowest unoccupied molecular orbital (LUMO) occupied the aromatic-imide units, whereas the highest occupied molecular orbital (HOMO) was mainly localized on the electron-donor carbazole moieties. The clear separation of the HOMO and LUMO could be conductive to obtaining a small ΔE_{ST}, promoting the up-conversion process from the triplet (T_1) to the singlet (S_1) energy levels. Besides, the calculated HOMO and LUMO energy levels of **OBN-AICz** were −5.43 and −2.31 eV, respectively. The corresponding energy gap (E_g) between the HOMO and LUMO energy levels was calculated to be 3.12 eV. Although the chiral unit made no contribution to both the HOMOs and LUMOs, CD and CPL activities could be detected due to chiral perturbation.

To further explore the structure of the obtained TADF enantiomers, the single-crystal structure of *S*-**OBN-AICz** was obtained successfully. As shown in Fig. 2 and Fig. S1 (ESI†), the absolute configurations, the intra- and intermolecular interactions, and the molecular packing modes of *S*-**OBN-AICz** were determined. As illustrated in Table S1 (ESI†), its single-crystal structure belongs to the monoclinic crystal system with the space group of $P2_1$. The crystal structure displayed a highly twisted conformation with dihedral angles between the two carbazoles and phenyl rings of 63.5° and 81.3°, respectively. Due to the asymmetry of the chiral moiety, the two carbazoles have different distances from their adjacent oxygen atoms on the **OBN**. The carbazole that is closer to the oxygen atom on **OBN** can form an intramolecular C–H···O hydrogen bond, while the other one that is farther away cannot form a hydrogen bond. The torsion angle of the carbazole can be limited by the C–H···O hydrogen bond between the oxygen atom on **OBN** and the C–H bond on the carbazole, leading to an obvious difference in dihedral angle. In addition, the large torsion angle between the donor and acceptor facilitates the effective

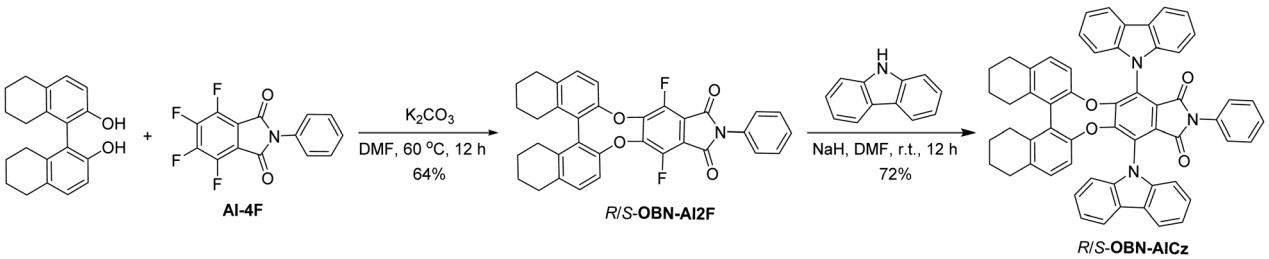

Scheme 1 Synthetic routes for the *R*/*S*-**OBN-AICz** enantiomers.

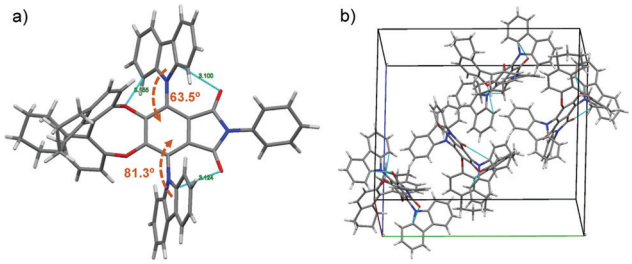

Fig. 2 (a) Single-crystal structure and (b) molecular packing mode in the unit cell of *S*-**OBN-AICz**.

spatial separation of the HOMO/LUMO, which is beneficial for achieving a small ΔE_{ST} value and efficient TADF properties.

Then, the thermal stabilities of the enantiomers were studied using thermal gravimetric analysis (TGA) under a nitrogen atmosphere at a heating rate of 10 °C min^{-1} (Fig. S2, ESI†). The enantiomers displayed excellent thermal stability with a decomposition temperature (T_d, corresponding to a 5% weight loss) of 419 °C for *R*-**OBN-AICz**. The glass transition temperature (T_g) is also one of the key material parameters of the emitter, which directly affects the process performance of the material. A high T_g can suppress crystallization or aggregation of the emitter during the deposition process, thereby forming a stable and uniform amorphous film. As shown in Fig. S3 (ESI†), the corresponding T_g was detected to be 220 °C using heating differential scanning calorimetry (DSC). The excellent thermal stabilities and morphological properties of the TADF enantiomers are necessary for fabricating OLED devices *via* vacuum evaporation.

The electrochemical properties of these TADF enantiomers were also studied using cyclic voltammetry (CV) in degassed anhydrous dichloromethane solvent. Owing to the almost identical properties of the enantiomers, *R*-**OBN-AICz** was chosen as the example (Fig. S4, ESI†). The HOMO energy levels were estimated to be −5.78 eV for *R*-**OBN-AICz**, from the onset of the oxidation spectrum with respect to that of ferrocene. Moreover, according to the absorption spectrum of the emitter in toluene, its corresponding E_g value was calculated to be 2.68 eV. Thus, the LUMO energy level of *R*-**OBN-AICz** was calculated to be −3.10 eV using the equation $E_{LUMO} = E_{HOMO} + E_g$. The suitable energy levels of this emitter in OLEDs are advantageous for charge injection (Table 1).

Photophysical properties

The UV-vis absorption and steady-state photoluminescence (PL) spectra of the emitter were measured. Taking *R*-**OBN-AICz** as an example in various solvents (Fig. S5, ESI†), this enantiomer showed a broad absorption band in the range of 370–460 nm, which could be assigned to the intramolecular charge-transfer (ICT) process from the donor carbazole to the acceptor aromatic-imide. And the emitter also showed a strong absorption band near 332 nm, which was related to the π–π* transition of **OBN** and the carbazole units. Furthermore, with an increase of the solvent polarity, the absorption spectra of the compound exhibited a slight change, while the PL spectra were more sensitive to different solvents. The PL spectra of *R*-**OBN-AICz** displayed a remarkable red-shift from blue (467 nm) in hexane to yellow (550 nm) in acetonitrile (Fig. S6, ESI†), confirming its typical ICT character in the excited state. Besides, the PLQY of *R*-**OBN-AICz** in toluene solution was measured to be 57%.

Subsequently, the AIE and twisted ICT properties of *R*-**OBN-AICz** were studied in THF/H_2O mixtures with various deionized water ratio fractions (f_w). As shown in Fig. 3c, *R*-**OBN-AICz** displayed the relatively weak PL emission in pure THF solution. Then, as the proportion of water in the system was increased from 0% to 60%, the emission intensity decreased dramatically and the emission peaks were red-shifted. This phenomenon might be attributed to the strong twisted ICT process and increased ISC rate caused by the increased polarity of the solvent. When the water fraction continued to be increased from f_w = 70% to f_w = 90%, a significant PL emission enhancement and blue-shifted emission peaks were observed. As shown in Fig. 3d, the PL intensity of *R*-**OBN-AICz** showed increase of 2.1 times from pure THF to f_w = 90% for the THF/H_2O mixture. Owing to aggregate formation, the intramolecular rotational motion was sufficiently restricted and the local environment became less polar. Therefore, the non-radiative decay of the excited state energy was prevented and the radiative decay was promoted, leading to a strong PL emission. These results demonstrated the AIE properties of *R*-**OBN-AICz**.

The PL spectra of *R*-**OBN-AICz** in a neat film were then studied at 77 K. As illustrated in Fig. S7 (ESI†), the fluorescence and phosphorescence spectra of the emitter showed an emission band centered at 529 and 539 nm, respectively. According to the onset wavelengths of its fluorescence and phosphorescence spectra at 77 K, the ΔE_{ST} value of *R*-**OBN-AICz** was calculated to be 0.08 eV, which could facilitate the RISC process from T_1 to S_1, resulting in efficient TADF. In order to simulate the emissive behaviour in OLEDs, the basic photophysical properties of *R*-**OBN-AICz** in a 3,3-di(9*H*-carbazol-9-yl)biphenyl (mCBP) doped film were further measured. As illustrated in Fig. 3a, the 13 wt% *R*-**OBN-AICz** doped film exhibited a

Table 1 Summary of photophysical, electrochemical and thermal properties of *R*-**OBN-AICz**

Compound	λ_{abs} [a] [nm]	λ_{fl} [b] [nm]	Φ_{PL} [c] [%]	τ [d] [μs]	HOMO/LUMO [e] [eV]	E_g [f] [eV]	ΔE_{ST} [eV]	T_d [°C]	T_g [°C]
R-**OBN-AICz**	290, 318, 332, 397	509	81	4.0	−5.78/−3.10	2.68	0.08	419	220

[a] Peaks of absorption spectra in toluene at room temperature. [b] Fluorescence spectra at room temperature measured in doped films. [c] Absolute PLQY measured in doped films using an integer sphere. [d] Delayed lifetimes were determined from the transient PL in doped films. [e] HOMO energy level measured from the oxidation potential in dichloromethane solution using cyclic voltammetry with ferrocene as the internal standard, and LUMO energy level calculated from $E_{HOMO} + E_g$. [f] Estimated from the onset of the absorption spectrum.

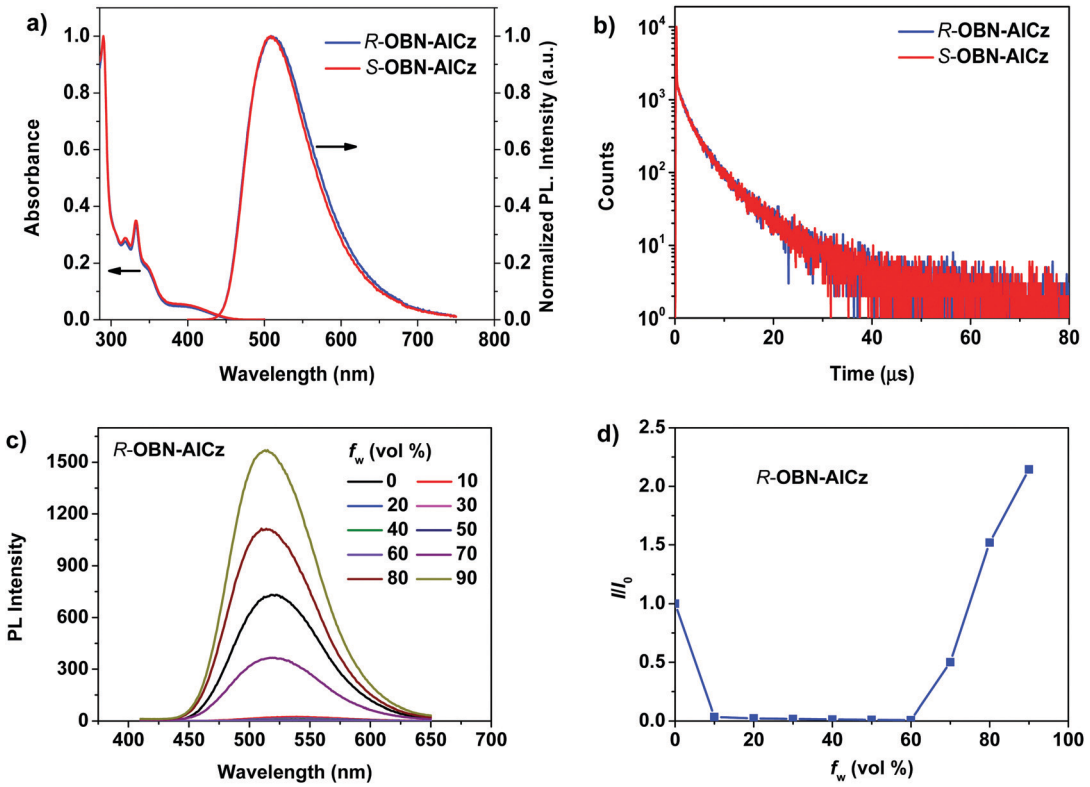

Fig. 3 (a) UV–vis absorption in toluene and PL spectra of *R*/*S*-**OBN-AICz** in doped films. (b) Temperature-dependent transient decay curves of *R*/*S*-**OBN-AICz** in doped films. (c) PL spectra of *R*-**OBN-AICz** in THF/H_2O mixtures with different water fraction (f_w) values. (d) Plots of the relative PL peak intensity (I/I_0) of the THF/H_2O mixture of *R*-**OBN-AICz**.

fluorescence peak centered at 509 nm, which has an obvious blue-shift compared with the pure film. And the doped film of *R*-**OBN-AICz** a high PLQY of 81% was demonstrated. Meanwhile, the transient PL decay curves of this doped film were also recorded at room temperature (Fig. 3b). It was found that the transient decay curve of *R*-**OBN-AICz** presented clear two exponential decay. The delayed lifetime of *R*-**OBN-AICz** was estimated to be 4.0 μs, which was related to the delayed fluorescence through RISC processes, illustrating its TADF properties. Moreover, the photophysical properties of *S*-**OBN-AICz** were also studied (Fig. 3a, b and Fig. S8, ESI†). It was found that the UV-vis absorption, PL and transient PL decay spectra of *S*-**OBN-AICz** were similar to those of *R*-**OBN-AICz**. These results demonstrate that chirality does not affect the molecular photophysical properties.

Chiroptical properties

We also investigated the chiroptical properties of *R*-**OBN-AICz** and *S*-**OBN-AICz** in the ground and excited states using electronic circular dichroism (ECD) and CPL spectra, respectively. As shown in Fig. 4a, the enantiomers exhibited a clear mirror-image ECD band in toluene. In the wavelength region below 325 nm, the strong Cotton effects could be attributed to the characteristic absorption of the chiral **OBN** moiety. Meanwhile, the weak Cotton effects in the long-wavelength region were assigned to the absorption of the ICT band from the carbazole donor to aromatic-imide moiety. These results revealed that the chirality was realized for these emitters through the chiral perturbation strategy. In addition, obvious mirror-image CPL

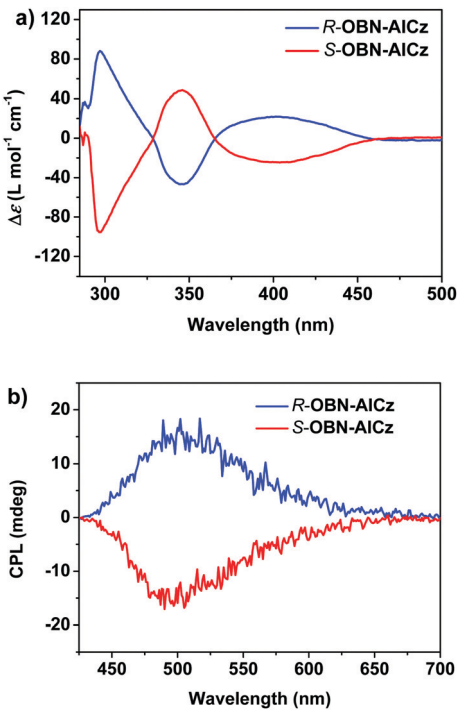

Fig. 4 (a) ECD and (b) CPL spectra of *R*-**OBN-AICz** and *S*-**OBN-AICz** in toluene.

spectra of *R*-**OBN-AICz** and *S*-**OBN-AICz** in toluene indicated their chiroptical properties in the excited state. As illustrated in Fig. 4b, *R*-**OBN-AICz** and *S*-**OBN-AICz** exhibited positive and negative CPL signals with g_{PL} values of $+2.6 \times 10^{-3}$ and -2.4×10^{-3}, respectively. These results indicate that the chiral perturbation strategy successfully imparts chirality to the TADF emitters. Moreover, the CPL signals of the enantiomers were also observed with g_{PL} values of $+2.6 \times 10^{-3}$ for *R*-**OBN-AICz** and -2.4×10^{-3} for *S*-**OBN-AICz** in doped films (Fig. S11 and S12, ESI†).

Electroluminescence properties

The electroluminescence (EL) properties of *R*-**OBN-AICz** and *S*-**OBN-AICz** were evaluated using mCBP as the host matrix of the emitting-layer (EML). First of all, four devices **A**–**D** were fabricated using 1,3,5-tri[(3-pyridyl)-phen-3-yl]benzene (TmPyPB), 1,3,5-tris(1-phenyl-1*H*-benzimidazol-2-yl)benzene (TPBi), 4,7-diphenyl-1,10-phenanthroline (Bphen) and 1,3-bis(3,5-dipyrid-3-ylphenyl)benzene (B3PYPB), respectively, as different electron-transporting layer (ETL) materials. These four series of OLED devices adopted the configurations of ITO/TAPC (40 nm)/mCBP (10 nm)/mCBP:13 wt% *R*-**OBN-AICz** (20 nm)/ETL (45 nm)/LiF (1 nm)/Al (100 nm). In these devices, TAPC (1,1-bis[(di-4-tolylamino)phenyl]cyclohexane) was used as the hole-transporting material, and mCBP was utilized as the exciton-blocking layer to confine the excitons within the EML. The results of their device performance are illustrated in Fig. S14–S18 (ESI†) and the relevant parameters are summarized in Table S2 (ESI†). Compared with the other three groups of devices, device **A** with TmPyPB as the ETL obtained the best overall performance with EQE_{max} = 17.5% and L_{max} = 11 610 cd m^{-2}.

We screened the thickness of each layer in the TmPyPB-based OLED devices to further optimize the device structures (Fig. S19–S23 and Table S3, ESI†). Finally, the best devices were

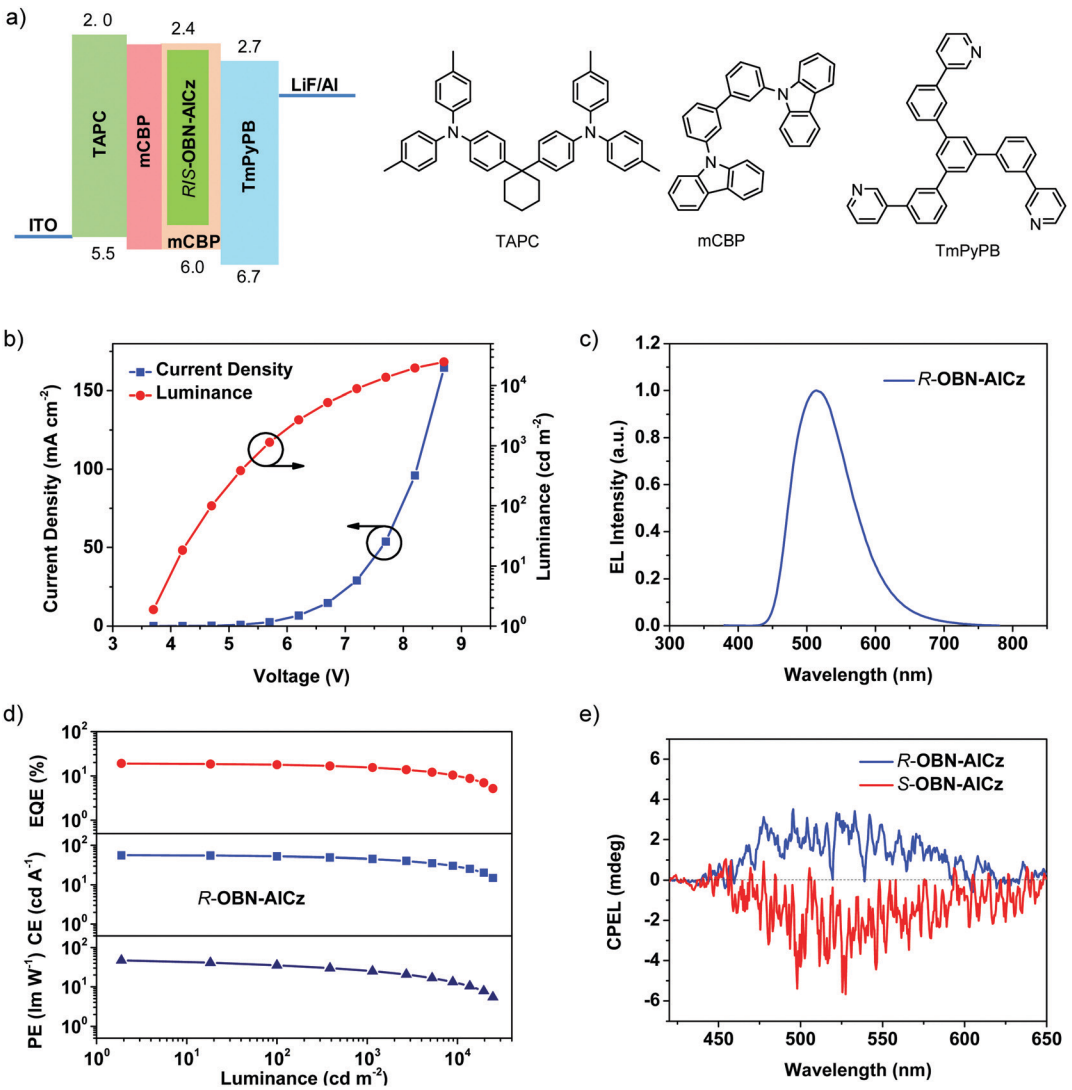

Fig. 5 (a) Device structure, energy level diagram and molecular structures of the materials employed in the optimized devices. (b) Current density–voltage–luminance (*J*–*V*–*L*) characteristics, (c) EL spectra, and (d) efficiency–luminance characteristics of the optimized *R*/*S*-**OBN-AICz**-based OLEDs. (e) CPEL spectra of the CP-OLEDs based on *R*-**OBN-AICz** and *S*-**OBN-AICz**.

Table 2 EL performances of the optimized *R*/*S*-**OBN-AICz**-based OLEDs

Emitter	$V_{turn\text{-}on}$[a] [V]	λ_{EL}[b] [nm]	EQE_{max}[c] [%]	CE_{max}[d] [cd A^{-1}]	PE_{max}[e] [lm W^{-1}]	L_{max}[f] [cd m^{-2}]
R-**OBN-AICz**	3.7	514	19.0	55.9	47.5	24 790
S-**OBN-AICz**	3.4	514	18.7	56.7	45.7	21 470

[a] Turn-on voltage at 1 cd m^{-2}. [b] EL peak wavelength. [c] Maximum external quantum efficiency (EQE). [d] Maximum current efficiency (CE). [e] Maximum power efficiency (PE). [f] Maximum luminance.

obtained with the following device configurations: ITO/TAPC (40 nm)/mCBP (10 nm)/mCBP:13 wt% *R*/*S*-**OBN-AICz** (15 nm)/TmPyPB (50 nm)/LiF (1 nm)/Al (100 nm) (Fig. 5a). The device performances including the current density–voltage–luminance characteristics, EL spectra, and efficiency *versus* luminance of the OLED devices are illustrated in Fig. 5b–d and Fig. S24–S26 (ESI†), and the detailed device performance parameters are summarized in Table 2. As shown in Fig. 5c, the *R*-**OBN-AICz**-based OLEDs could emit EL emission with the peak centered at 514 nm and Commission Internationale de l'Éclairage (CIE) color coordinates of (0.27, 0.52). Furthermore, an EQE_{max} of 19.0%, a CE_{max} of 55.9 cd A^{-1}, a PE_{max} of 47.5 lm W^{-1}, and an L_{max} of 24 790 cd m^{-2} were achieved in the *R*-**OBN-AICz**-based OLED devices. Similarly, the *S*-**OBN-AICz**-based OLED devices showed EQE_{max}, CE_{max}, PE_{max}, and L_{max} values of 18.7%, 56.7 cd A^{-1}, 45.7 lm W^{-1}, and 21470 cd m^{-2}, respectively. It was further found that the corresponding devices exhibited a low turn-on voltage of 3.7 V for the *R*-**OBN-AICz**-based OLED and 3.4 V for the *S*-**OBN-AICz**-based OLED at a luminance of 1 cd m^{-2}, indicating efficient carrier injection and transport.

Considering the CPL properties of the enantiomers, the CP-OLEDs were fabricated using *R*-**OBN-AICz** and *S*-**OBN-AICz** as emitters to investigate the CPEL characteristics. As illustrated in Fig. 5e, the CP-OLEDs demonstrated clear mirror-image CPEL activities, keeping the direction consistent with the CPL signals. And these devices displayed opposing electroluminescence dissymmetry factor (g_{EL}) values of $+4.7 \times 10^{-4}$ and -6.5×10^{-4} for the *R*-**OBN-AICz**- and *S*-**OBN-AICz**-based devices, respectively. The above results confirmed that the direct combination of chiral moieties and efficient TADF moieties could make the emitters produce CP signals in both photoluminescence and electroluminescence processes.

Conclusions

In summary, we have successfully developed a pair of aromatic-imide-based TADF enantiomers, namely *R*-**OBN-AICz** and *S*-**OBN-AICz**, by directly combining chiral units with TADF skeletons. These enantiomers displayed excellent TADF properties with a small ΔE_{ST} value of low to 0.08 eV, a high PLQY of up to 81%, as well as obvious AIE properties. Moreover, the TADF enantiomers exhibited clear mirror-image CD and CPL activities with $|g_{PL}|$ values of up to 2.6×10^{-3}. Finally, high-efficiency CP-OLEDs were fabricated by adopting *R*-**OBN-AICz** and *S*-**OBN-AICz** as emitters. The fabricated CP-OLEDs showed a high EQE_{max} of 19.0% and an L_{max} of 24 790 cd m^{-2}. Notably, CPEL activities with opposing g_{EL} signals were detected in the CP-OLEDs based on *R*/*S*-**OBN-AICz**. These results can provide a convenient method to develop aromatic-imide-based TADF enantiomers, which will be helpful for the further development of high-efficiency CPEL materials.

Experimental section

The synthetic routes to the pair of TADF enantiomers *R*/*S*-**OBN-AICz** are outlined in Scheme 1. All experiments were performed under an argon atmosphere. All reagents were purchased from commercial sources and used without further purification. Compound **AI4F** was synthesized according to the literature.[15]

Preparation procedure for *R*-OBN-AI2F

A solution of **AI-4F** (3.0 g, 10.2 mmol), *R*-5,5′,6,6′,7,7′,8,8′-octahydro-1,1′-2-naphthol (3.0 g, 10.2 mmol) and potassium carbonate (2.9 g, 21.0 mmol) in dry DMF (40.0 mL) was stirred for 12 h at 60 °C. After cooling to room temperature, the mixture was extracted using ethyl acetate and washed with saturated brine. The combined organic layer was dried with anhydrous $MgSO_4$ and filtered, then concentrated to obtain the crude compound. Further purification was carried out *via* column chromatography on silica gel using CH_2Cl_2/petroleum ether as the eluent to afford a white powder with a yield of 64%. ^{1}H NMR (500 MHz, $CDCl_3$): δ 7.49 (t, J = 7.7 Hz, 2H), 7.43–7.36 (m, 3H), 7.14 (d, J = 8.3 Hz, 2H), 6.99 (d, J = 8.2 Hz, 2H), 2.89–2.78 (m, 4H), 2.72–2.61 (m, 2H), 2.43–2.39 (m, 2H), 1.84–1.81 (m, 6H), 1.68–1.64 (m, 2H). ^{13}C NMR (126 MHz, $CDCl_3$): δ 162.7, 149.6, 148.3, 146.2, 145.88, 145.85, 137.3, 136.4, 131.0, 130.6, 129.4, 129.2, 128.4, 126.5, 118.3, 112.0, 29.3, 27.6, 22.6, 22.5. HRMS m/z calcd for $C_{34}H_{26}O_4NF_2$ [M + H]: 550.1824, found: 550.1814.

Preparation procedure for *R*-OBN-AICz

A solution of carbazoles (1.5 g, 9.0 mmol) in dry DMF (20.0 mL) was stirred for 5 min at room temperature, and then sodium hydride (0.24 g, 10.0 mmol) was added to the solution. After another 30 min, *R*-**OBN-AI2F** (2.2 g, 4.0 mmol) was added to the mixture and stirred for 12 h at room temperature. Then the suspension mixture was poured into water, and the aqueous layer was extracted using ethyl acetate. The combined organic layers were washed with saturated brine and concentrated under vacuum. Further purification was carried out *via* column chromatography on silica gel using CH_2Cl_2/petroleum ether as the eluent to afford a green powder with a yield of 72%. ^{1}H NMR (500 MHz, $CDCl_3$): δ 8.19 (d, J = 7.5 Hz, 2H), 8.13 (d, J = 6.9 Hz, 2H), 7.50 (t, J = 7.1 Hz, 2H), 7.36 (t, J = 7.2 Hz, 2H),

7.32–7.26 (m, 5H), 7.24–7.19 (m, 3H), 7.16 (d, J = 7.7 Hz, 3H), 6.90 (d, J = 7.7 Hz, 4H), 6.32 (d, J = 8.1 Hz, 2H), 2.74–2.72 (m, 4H), 2.47–2.44 (m, 2H), 2.18–2.15 (m, 2H), 1.74–1.70 (m, 6H), 1.50–1.48 (m, 2H). ^{13}C NMR (126 MHz, $CDCl_3$): δ 162.9, 154.7, 149.8, 141.2, 141.0, 137.1, 135.8, 131.1, 130.1, 129.3, 128.6, 127.9, 127.7, 126.2, 126.0, 125.8, 124.4, 124.0, 120.8, 120.6, 120.43, 120.35, 117.9, 110.3, 109.6, 29.2, 27.4, 22.6, 22.4. HRMS m/z calcd for $C_{58}H_{42}N_3O_4$ [M + H]: 844.3170, found: 844.3157.

***S*-OBN-AICz** was prepared using the above synthetic routes. ^{1}H NMR (500 MHz, $CDCl_3$): δ 8.19 (d, J = 7.7 Hz, 2H), 8.14 (d, J = 7.3 Hz, 2H), 7.50 (t, J = 7.5 Hz, 2H), 7.36 (t, J = 7.4 Hz, 2H), 7.32–7.26 (m, 5H), 7.24–7.20 (m, 3H), 7.17 (d, J = 8.0 Hz, 3H), 6.90 (d, J = 7.9 Hz, 4H), 6.33 (d, J = 8.2 Hz, 2H), 2.75–2.73 (m, 4H), 2.49–2.43 (m, 2H), 2.20–2.15 (m, 2H), 1.75–1.69 (m, 6H), 1.51–1.47 (m, 2H). ^{13}C NMR (126 MHz, $CDCl_3$): δ 162.9, 154.7, 149.8, 141.2, 141.0, 137.1, 135.8, 131.1, 130.1, 129.3, 128.6, 127.9, 127.7, 126.2, 126.0, 125.8, 124.4, 124.0, 120.8, 120.6, 120.42, 120.35, 117.9, 110.3, 109.6, 29.2, 27.4, 22.6, 22.4. HRMS m/z calcd for $C_{58}H_{42}N_3O_4$ [M + H]: 844.3170, found: 844.3154.

Author contributions

This manuscript was written through the contributions of all authors. All authors have given approval to the final version of the manuscript.

Conflicts of interest

There are no conflicts to declare.

Acknowledgements

We thank the National Natural Science Foundation of China (22122111, 91956119, and 92056109), the Beijing National Laboratory for Molecular Sciences (BNLMS-CXXM-202105) and the Youth Innovation Promotion Association CAS (2019034) for financial support.

References

1 (*a*) Y. Zhang and G. B. Schuster, *J. Org. Chem.*, 1995, **60**, 7192; (*b*) W. F. Jager, B. D. Lange and B. L. Feringa, *Science*, 1996, **273**, 1686; (*c*) J. Sherson, H. Krauter, R. Olsson, B. Julasgaard, K. Hammerer, I. Cirac and E. Polzik, *Nature*, 2006, **443**, 557; (*d*) S. Relaix, C. Bourgerette and M. Mitov, *Appl. Phys. Lett.*, 2006, **89**, 251907; (*e*) M. C. Heffern, L. M. Matosziuk and T. J. Meade, *Chem. Rev.*, 2014, **114**, 4496; (*f*) J. Kumar, T. Nakashima and T. Kawai, *J. Phys. Chem. Lett.*, 2015, **6**, 3445; (*g*) R. Clarke, K. Ho, A. Alsimaree, O. Woodford, P. Waddell, J. Bogaerts, W. Herrebout, J. Knight, R. Pal, T. Penfold and M. Hall, *ChemPhotoChem*, 2017, **1**, 513; (*h*) J. Yan, F. Ota, B. A. San Jose and K. Akagi, *Adv. Funct. Mater.*, 2017, **27**, 1604529.

2 (*a*) R. Carr, N. H. Evans and D. Parker, *Chem. Soc. Rev.*, 2012, **41**, 7673; (*b*) M. C. Heffern, L. M. Matosziuk and T. J. Meade, *Chem. Rev.*, 2014, **114**, 4496; (*c*) E. Yashima, N. Ousaka, D. Taura, K. Shimomura, T. Ikai and K. Maeda, *Chem. Rev.*, 2016, **116**, 13752; (*d*) M. Li, W.-B. Lin, L. Fang and C.-F. Chen, *Acta Chim. Sin.*, 2017, **75**, 1150.

3 (*a*) Z. Yang, Z. Mao, Z. Xie, Y. Zhang, S. Liu, J. Zhao, J. Xu, Z. Chi and M. P. Aldred, *Chem. Soc. Rev.*, 2017, **46**, 915; (*b*) M. Y. Won and E. Zysman-Colman, *Adv. Mater.*, 2017, **29**, 1605444; (*c*) Y. Liu, C. Li, Z. Ren, S. Yan and M. R. Bryce, *Nat. Rev. Mater.*, 2018, **3**, 18020; (*d*) S. K. Jeon, H. Lee, K. S. Yook and J. Y. Lee, *Adv. Mater.*, 2019, **31**, 1803524.

4 (*a*) J. R. Brandt, F. Salerno and M. J. Fuchter, *Nat. Rev. Chem.*, 2017, **1**, 0045; (*b*) D.-W. Zhang, M. Li and C.-F. Chen, *Chem. Soc. Rev.*, 2020, **49**, 1331; (*c*) M. Li, M.-Y. Wang, Y.-F. Wang, L. Feng and C.-F. Chen, *Angew. Chem., Int. Ed.*, 2021, **60**, 20728.

5 E. Peeters, M. Christiaans, R. Janssen, H. Schoo, H. Dekkers and E. W. Meijer, *J. Am. Chem. Soc.*, 1997, **119**, 9909.

6 (*a*) D.-M. Lee, J.-W. Song, Y.-J. Lee, C.-J. Yu and J.-H. Kim, *Adv. Mater.*, 2017, **29**, 1700907; (*b*) J.-H. Jung, D.-M. Lee, J.-H. Kim and C.-J. Yu, *J. Mater. Chem. C*, 2018, **6**, 726; (*c*) L. Yang, Y. Zhang, X. Zhang, N. Li, Y. Quan and Y. Cheng, *Chem. Commun.*, 2018, **54**, 9663; (*d*) Y. Zhang, X. Zhang, H. Zhang, Y. Xiao, Y. Quan, S. Ye and Y. Cheng, *J. Phys. Chem. C*, 2019, **123**, 24746; (*e*) L. Wan, J. Wade, F. Salerno, O. Arteaga, B. Laidlaw, X. Wang, T. Penfold, M. J. Fuchter and A. J. Campbell, *ACS Nano*, 2019, **13**, 8099.

7 (*a*) T.-Y. Li, Y.-M. Jing, X. Liu, Y. Zhao, L. Shi, Z. Y. Tang, Y.-X. Zheng and J.-L. Zuo, *Sci. Rep.*, 2015, **5**, 14912; (*b*) F. Zinna, U. Giovanella and L. D. Bari, *Adv. Mater.*, 2015, **27**, 1791; (*c*) J. R. Brandt, X. Wang, Y. Yang, A. J. Campnell and M. J. Fuchter, *J. Am. Chem. Soc.*, 2016, **138**, 9743; (*d*) J. Han, S. Guo, J. Wang, L. Wei, Y. Zhuang, S. Liu, Q. Zhao, X. Zhang and W. Huang, *Adv. Opt. Mater.*, 2017, **5**, 1700359; (*e*) Z.-P. Yan, K. Liao, H.-B. Han, J. Su, Y.-X. Zheng and J.-L. Zuo, *Chem. Commun.*, 2019, **55**, 8215; (*f*) Z.-P. Yan, X.-F. Luo, W.-Q. Liu, Z.-G. Wu, X. Liang, K. Liao, Y. Wang, Y.-X. Zheng, L. Zhou, J.-L. Zuo, Y. Pan and H. Zhang, *Chem. – Eur. J.*, 2019, **25**, 5672; (*g*) G. Fu, Y. He, W. Li, B. Wang, X. Lü, H. He and W.-Y. Wong, *J. Mater. Chem. C*, 2019, **7**, 13743; (*h*) Y. Chen, X. Li, N. Li, Y. Quan, Y. Cheng and Y. Tang, *Mater. Chem. Front.*, 2019, **3**, 867.

8 (*a*) Y. Wang, Y. Zhang, W. Hu, Y. Quan, Y. Li and Y. Cheng, *ACS Appl. Mater. Interfaces*, 2019, **11**, 26165; (*b*) M. Li, Y.-F. Wang, D. Zhang, L. Duan and C.-F. Chen, *Angew. Chem., Int. Ed.*, 2020, **59**, 3500; (*c*) Z.-L. Tu, Z.-P. Yan, X. Liang, L. Chen, Z.-G. Wu, Y. Wang, Y.-X. Zheng, J.-L. Zuo and Y. Pan, *Adv. Sci.*, 2020, **7**, 2000804; (*d*) S.-Y. Yang, Y.-K. Wang, C.-C. Peng, Z.-G. Wu, S. Yuan, Y.-J. Yu, H. Li, T.-T. Wang, H.-C. Li, Y.-X. Zheng, Z.-Q. Jiang and L.-S. Liao, *J. Am. Chem. Soc.*, 2020, **142**, 17756; (*e*) F. Ni, C.-W. Huang, Y. Tang, Z. Chen, Y. Wu, S. Xia, X. Cao, J.-H. Hsu, W.-K. Lee, K. Zheng, Z. Huang, C.-C. Wu and C. Yang, *Mater. Horiz.*, 2021, **8**, 547; (*f*) Y.-F. Wang, M. Li,

J.-M. Teng, H.-Y. Zhou and C.-F. Chen, *Adv. Funct. Mater.*, 2021, **31**, 2106418; (*g*) Y.-F. Wang, M. Li, J.-M. Teng, H.-Y. Zhou, W.-L. Zhao and C.-F. Chen, *Angew. Chem., Int. Ed.*, 2021, **60**, 23619.

9 L. Frédéric, A. Desmarchelier, L. Favereau and G. Pieters, *Adv. Funct. Mater.*, 2021, **31**, 2010281.

10 (*a*) M. Li, Y. Liu, R. Duan, X. Wei, Y. Yi, Y. Wang and C.-F. Chen, *Angew. Chem., Int. Ed.*, 2017, **56**, 8818; (*b*) M. Li, Y.-F. Wang, D.-W. Zhang, D. Zhang, Z.-Q. Hu, L. Duan and C.-F. Chen, *Sci. China Mater.*, 2021, **64**, 899; (*c*) L. Zhang, Y.-F. Wang, M. Li, Q.-Y. Gao and C.-F. Chen, *Chin. Chem. Lett.*, 2021, **32**, 740.

11 (*a*) M. Li, S.-H. Li, D. Zhang, M. Cai, L. Duan, M.-K. Fung and C.-F. Chen, *Angew. Chem., Int. Ed.*, 2018, **57**, 2889; (*b*) Y.-F. Wang, H.-Y. Lu, C. Chen, M. Li and C.-F. Chen, *Org. Electron.*, 2019, **70**, 71.

12 (*a*) F. Song, Z. Xu, Q. Zhang, Z. Zhao, H. Zhang, W. Zhao, Z. Qiu, C. Qi, H. Zhang, H. H. Y. Sung, I. D. Williams, J. W. Y. Lam, Z. Zhao, A. Qin, D. Ma and B. Z. Tang, *Adv. Funct. Mater.*, 2018, **28**, 1800051; (*b*) S. Sun, J. Wang, L. Chen, R. Chen, J. Jin, C. Chen, S. Chen, G. Xie, C. Zheng and W. Huang, *J. Mater. Chem. C*, 2019, **7**, 14511; (*c*) L. Frédéric, A. Desmarchelier, R. Plais, L. Lavnevich, G. Muller, C. Villafuerte, G. Clavier, E. Quesnel, B. Racine, S. Meunier-Della-Gatta, J.-P. Dognon, P. Thuéry, J. Crassous, L. Favereau and G. Pieters, *Adv. Funct. Mater.*, 2020, **30**, 2004838.

13 (*a*) Z.-G. Wu, H. B. Han, Z.-P. Yan, X.-F. Luo, Y. Wang, Y.-X. Zheng, J.-L. Zuo and Y. Pan, *Adv. Mater.*, 2019, **31**, 1900524; (*b*) Z.-G. Wu, Z.-P. Yan, X.-F. Luo, L. Yuan, W.-Q. Liang, Y. Wang, Y.-X. Zheng, J.-L. Zuo and Y. Pan, *J. Mater. Chem. C*, 2019, **7**, 7045; (*c*) Y. Xu, Q. Wang, X. Cai, C. Li and Y. Wang, *Adv. Mater.*, 2021, **33**, 2100652; (*d*) F.-M. Xie, J.-X. Zhou, X.-Y. Zeng, Z.-D. An, Y.-Q. Li, D.-X. Han, P.-F. Duan, Z.-G. Wu, Y.-X. Zheng and J.-X. Tang, *Adv. Opt. Mater.*, 2021, **9**, 2100017.

14 Y.-F. Wang, C. Chen, L. Cui, J.-M. Teng, M. Li, H.-Y. Lu and C.-F. Chen, *Org. Electron.*, 2021, **99**, 106355.

15 X. Liu, Y.-F. Wang, M. Li, Y. Zhu and C.-F. Chen, *Org. Electron.*, 2021, **88**, 106017.

